

Reconstruction of finite deep sub-wavelength nanostructures by Mueller-matrix scattered-field microscopy

CAI WANG,¹ XIUGUO CHEN,^{1,*} CHAO CHEN,¹ SHENG SHENG,¹
LIXUAN SONG,¹ HONGGANG GU,¹ HAO JIANG,¹ CHUANWEI
ZHANG,¹ AND SHIYUAN LIU^{1,2}

¹State Key Laboratory of Digital Manufacturing Equipment and Technology, Huazhong University of Science and Technology, Wuhan, Hubei 430074, China

²shyliu@hust.edu.cn

*xiuguochen@hust.edu.cn

Abstract: Computational super-resolution is a novel approach to break the diffraction limit. The Mueller matrix, which contains full-polarization information about the morphology and structure of a sample, can add super-resolution information and be a promising way to further enhance the resolution. Here we proposed a new approach called Mueller-matrix scattered-field microscopy (MSM) that relies on a computational reconstruction strategy to quantitatively determine the geometrical parameters of finite deep sub-wavelength nanostructures. The MSM adopts a high numerical-aperture objective lens to collect a broad range of spatial frequencies of the scattered field of a sample in terms of Mueller-matrix images. A rigorous forward scattering model is established for MSM, which takes into account the vectorial nature of the scattered field when passing through the imaging system and the effect of defocus in the measurement process. The experimental results performed on a series of isolated Si lines have demonstrated that MSM can resolve a feature size of $\lambda/16$ with a sub-7 nm accuracy. The MSM is fast and has a great measurement accuracy for nanostructures, which is expected to have a great potential application for future nanotechnology and nanoelectronics manufacturing.

© 2021 Optical Society of America under the terms of the [OSA Open Access Publishing Agreement](#)

1. Introduction

Optical microscopy is convenient and nondestructive for characterizing various samples and has a wide range of applications. However, its resolution is inherently limited by the well-known Abbe diffraction limit, i.e., resolution cannot exceed half of the illumination wavelength λ . To break this limit, several approaches have been proposed over the past decades. The near-field scanning optical microscopy (NSOM) is a typical near-field super-resolution technique that collects the evanescent waves by scanning with a sharp tip [1–3]. However, NSOM is normally limited to surface studies and is also time-consuming to scan large sample areas. As for the far-field super-resolution, there are two major methods, one of which is the deterministic technique (such as the stimulated emission depletion microscopy [4]), and the other is the stochastic technique (such as the photo-activated localization microscopy [5]). And these methods are usually applicable to biological samples. However, the need of special dyes hinders its applications to non-fluorescence samples such as nanostructures in semiconductor industry. Other label-free far-field super-resolution techniques, such as structured-illumination microscopy [6,7], improve the resolution only up to about a factor of two beyond the diffraction limit. On the other hand, as the nanotechnology and nanoelectronics manufacturing techniques continue to progress, sub-wavelength nanostructures are widely used in current semiconductor devices [8,9], solar cells [10], photonic crystal waveguides [11], metasurfaces [12], etc. Consequently, fast and

nondestructive characterization of nanostructures, especially those with deep sub-wavelength size, still remains a challenge for existing testing tools.

Another label-free far-field super-resolution technique that can be termed as computational super-resolution has been recently developed with a great potential for realizing fast and nondestructive characterization of features at deep sub-wavelength scale [13–16]. The computational super-resolution technique first tries to collect more scattering information from a sample and then reconstructs the sample profile by fitting the collected data to an established forward scattering model. Arhab et al. developed a profilometry setup based on the optical diffraction tomography. They measured the amplitude and phase of the scattered field and took the multiple scattering into account in the forward model, achieving the characterization of subwavelength features beyond the diffraction limit [13]. Qin et al. developed a scatterfield microscopy that enables the measurement of deep sub-wavelength features by acquiring images of sample at different defocus positions and modeling a broad range of spatial frequencies of scattered field [14]. Chen et al. proposed an image-inversion approach by combining a full-wave modeling of a confocal laser scanning microscopy and demonstrated a 35 nm edge-to-edge resolution [15].

It is noted that the reported works about computational super-resolution typically exploits information about the amplitude, phase, spatial frequency, and different defocus positions of the scattered field. However, another dimension of the scattered field, the polarization, can also provide valuable information and may be a promising way to further enhance the resolution [17–20]. Serrels et al. pointed out by experiments that the resolution of a confocal microscopy could be improved along a specific direction that depends on the polarization direction of illumination [17]. Hafi et al. used fluorescent polarization modulation and a sparsity deconvolution algorithm to achieve a sub-diffraction resolution [18]. Zhanghao et al. developed a new technique called super-resolution dipole orientation mapping that relies on the fluorescent dipole orientation information, and it combined polarization modulation to yield super-resolution [19]. Nevertheless, it is worth pointing out that those works only utilized a single or a specific polarization state of the illumination or scattered-field. To the best of our knowledge, the exploration of the Mueller matrix, which contains all information regarding the scatter that one can extract from a linear polarization scattering, to achieve super-resolution has not been reported yet.

In this work, by taking advantage of the full-polarization information of the scattered-field, we propose a new approach called Mueller-matrix scattered-field microscopy (MSM), which is capable of quantitatively determine the geometrical parameters of finite deep sub-wavelength nanostructures. The experimental setup of MSM employs a high numerical-aperture (NA) objective lens to collect a broad range of spatial frequencies of the scattered field in terms of Mueller-matrix images. A rigorous forward scattering model is established for MSM to reconstruct nanostructures, which takes account of the vectorial nature of the scattered field when passing through the imaging system and the effect of defocus in the measurement process. The experimental results performed on a series of isolated Si lines demonstrate that the proposed MSM can resolve a feature size of $\lambda/16$ with a sub-7 nm accuracy.

2. Experimental setup

Figure 1 presents the schematic of MSM, which consists of an illuminating light path indicated by the red arrow and an imaging light path indicated by the blue arrow, respectively. For the illuminating light path, a laser source with a wavelength of 633 nm is employed. The light passes through a rotating diffuser and is reflected by a rotatable mirror. Then the light passes through the polarization state generator (PSG) consisting of a polarizer and a phase retarder. Next, after passing through a non-polarizing beam splitter BS and lens L_1 , the light is focused on the back focal plane (BPF) of the objective lens (OB, Zeiss Epiplan-Apochromat 50 \times with NA of 0.95). After passing through the OB, a parallel light illuminates the sample with uniform intensity over

the spot. Moreover, we can rotate the mirror to change the position of the focal point on BPF, then the incident angle of illuminating light is also changed.

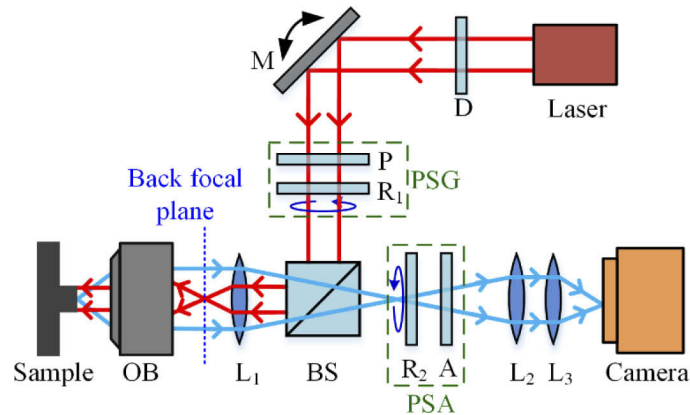


Fig. 1. The schematic of the developed Mueller-matrix scattered-field microscope. D: diffuser; M: mirror; P: polarizer; R_1 , R_2 : phase retarder; BS: beam splitter; OB: objective lens; A: analyzer; $L_1 \sim L_3$: lenses.

As for the imaging light path, the scattered light from the sample is collected by OB and passes successively through lens L_1 and BS. Then the scattered light passes through the polarization state analyzer (PSA) consisting of an analyzer and another phase retarder. The OB, L_1 , L_2 , and L_3 form two $4-f$ imaging systems, and finally the sample is imaged onto the camera. Note that, the phase retarders in PSG and PSA are both kept rotating during the measurement to generate different combinations of polarization states [21]. As a result, all 16 images of the Mueller-matrix of the sample can be acquired in a single measurement. For details about calibration of MSM, please refer to Section 1 of Supplement 1.

To demonstrate the capability of MSM for measuring finite deep subwavelength nanostructures, a series of isolated Si lines on a Si substrate with different dimensions has been prepared by

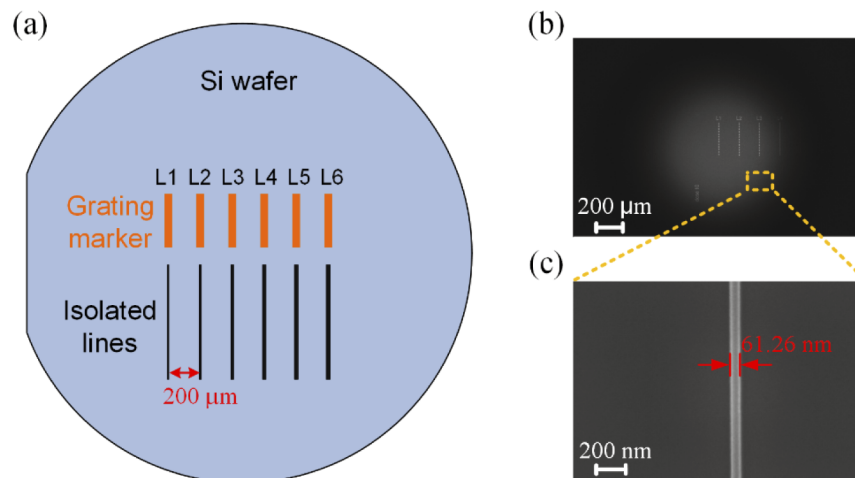


Fig. 2. (a) The layout of the isolated Si lines on the Si wafer; (b) The SEM micrograph of the investigated isolated Si lines; (c) The SEM micrograph of the line with a nominal width of 60 nm.

e-beam lithography followed by dry etching. As schematically shown in Fig. 2(a), we design six lines named L1 ~ L6 with a nominal width increases from 20 nm to 120 nm in a 20 nm interval and a nominal height of 50 nm. Grating markers are designed on the top of each line to make it easy to locate those lines. These lines are spaced 200 μm apart to ensure that they wouldn't affect each other during the measurement, therefore each line can be seen as an isolated structures. Figure 2(b) and Fig. 2(c) show the scanning-electron microscopy (SEM) micrograph of one of the fabricated isolated line samples. Note that the above isolated Si lines represent an extreme case of the finite deep subwavelength nanostructures. It can be expected that the proposed approach is also applicable to other finite subwavelength features.

3. Forward model and inverse reconstruction

Figure 3 illustrates the diagram of the forward modeling principle in MSM. Considering that the vectorial nature of the scattered field is taken into account as well as the high-NA objective lens employed in MSM, the vectorial diffraction theory is adopted in the forward modeling [22–24]. As shown in Fig. 3, the forward modeling in MSM consists of four parts: illuminating, scattering, propagating, focusing. Firstly, for the illuminating and scattering, the Maxwell's equation describing the interaction between the incident light and the sample is solved by a numerical solution method [25]. Then, for the scattered light propagating through the imaging system, i.e., from the entrance pupil to the exit pupil, only part of scattered light can be collected and propagate to the image plane. During this process, the orientation of the electric field of the scattered light will change along with the change of wave vector. Besides, the amplitude of the electric field will also change due to the amplification effect of the imaging system. The effect of defocus is also included in the forward model. Detailed derivations of the formula for the electric field on the entrance and exit pupil are appended in Section 2 of Supplement 1. Finally, for the focusing on the image plane, we use the Debye-Wolf integral to calculate the images as follows [22,23]

$$\mathbf{E}^{\text{image}}(x, y, z) = -\frac{i}{\lambda} \iint_{\Omega} \frac{\mathbf{E}^{\text{exit}}(r_x, r_y)}{r_z} e^{ik(r_x x + r_y y + r_z z)} dr_x dr_y, \quad (1)$$

where $k = 2\pi/\lambda$ is the wave number; λ is the illuminating wavelength; (r_x, r_y, r_z) is the unit wave vector of the scattered light leaving from the exit pupil; i is the imaginary unit defined as $i^2 = -1$; $\mathbf{E}^{\text{exit}}(r_x, r_y)$ is the electric field vector of the scattered light leaving from the exit pupil with the unit wave vector (r_x, r_y, r_z) ; Ω denotes the integration area, i.e., the solid angle limited by the exit pupil. Subsequently, calculating the electric field distribution on the image plane under the illuminating light with different polarization states, the Mueller-matrix image is obtained [26].

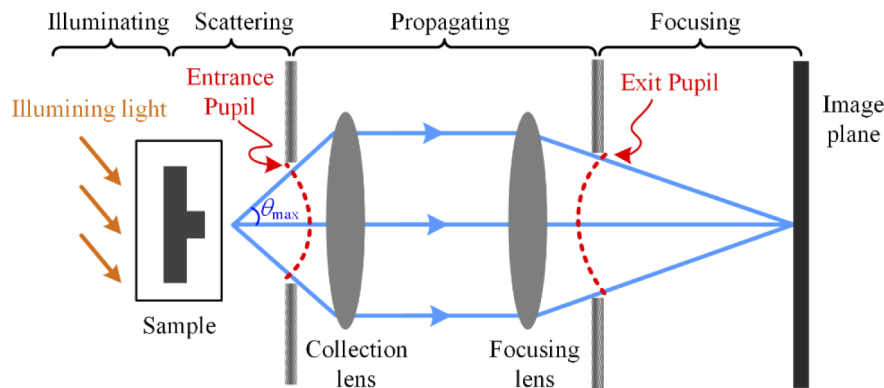


Fig. 3. The forward modeling principle in MSM.

Based on the established forward model, the reconstruction of a nanostructure is realized by solving an inverse scattering problem [27,28]. We use ξ to denote a vector consisting of the model parameters that describe geometrical parameters of the sample or measurement configurations. The ξ is varied and the corresponding Mueller-matrix image is calculated by the established forward model, with the objective to find the ξ whose calculated Mueller-matrix image can best match the measured one. Specifically, the optimal ξ is obtained by minimizing a chi-square value defined by

$$\chi^2 = \frac{1}{15K - P} \sum_{k=1}^K \sum_{i,j=1}^4 \left[\frac{m_{ij,k}^{mea} - m_{ij,k}^{cal}(\xi)}{\sigma(m_{ij,k})} \right]^2, \quad (2)$$

where k denotes the k th pixel with the total number of K ; i and j denote all the Mueller-matrix elements except m_{11} (normalized to m_{11}); $m_{ij,k}^{mea}$ denotes the measured Mueller-matrix image; $m_{ij,k}^{cal}(\xi)$ denotes the Mueller-matrix image calculated by the forward model with the input of ξ ; P denotes the number of dimension of ξ , and $\sigma(m_{ij,k})$ denotes the estimated standard deviation of measured Mueller-matrix images. We use the nonlinear least-squares regression method such as the Levenberg-Marquardt algorithm [29] to iteratively solve Eq. (2). In addition, the fitting procedure delivers 95% confidence limits of $1.96 \times \chi \times \sqrt{C_{ii}}$ for the fitting parameters, where $\sqrt{C_{ii}}$ is the i th diagonal element of the variance-covariance matrix associated with the fitting parameters.

4. Results and discussion

4.1. Simulation analysis

We first perform a simulation analysis to examine the sensitivity of MSM for the measurement of finite subwavelength nanostructures. Similar to the isolated structures in Fig. 2, Fig. 4 shows the cross-section profile of an isolated Si line on the Si substrate examined in simulation, which has a linewidth $W = 100$ nm and a line height $H = 50$ nm. The refractive index of Si refers to [30]. The wavelength is set to be 633 nm. The numerical-aperture (NA) and the magnification factor of the imaging system are set to 0.95 and 18 \times , respectively, which are identical to those in MSM.

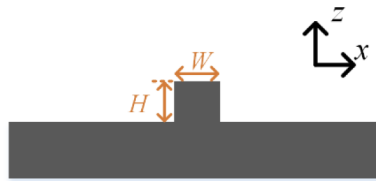


Fig. 4. The single Si line on the Si substrate structure examined in simulation.

To estimate the sensitivity, we define a *RMSE* to quantify variation of the Mueller-matrix images when the width W or the height H of the examined sample is changed, which is given as follows

$$RMSE = \sqrt{\frac{1}{15K} \sum_{k=1}^K \sum_{i,j=1}^4 [m_{ij,k} - m'_{ij,k}]^2} \quad (3)$$

where m and m' represents the Mueller-matrix elements of the original and changed examined sample, respectively; k represents k th pixel with a total number of K in Mueller-matrix image. Figure 5(a) shows the *RMSE* of the W changes by 1 nm, and Fig. 5(b) shows the *RMSE* of the H changes by 1 nm at different incident angles. As is known, the variation indicates measurement sensitivity and a large variation corresponds a high sensitivity. As can be observed, we can derive

that for both W and H , the sensitivity is high and nearly constant within 0° to about 20° , and decreases significantly as the incident angle increases above about 20° . This is primarily due to that as the angle of incidence increases, part of high spatial frequency information of the scattered field will exceed the collection range of the objective lens. And it causes the sensitivity decrease.

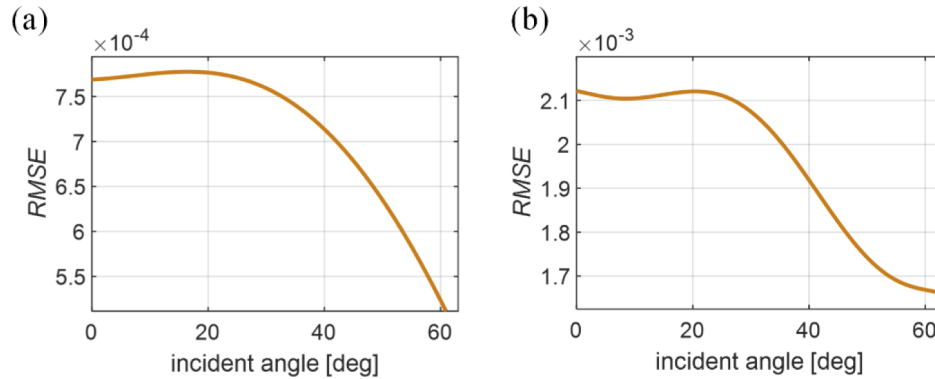


Fig. 5. The sensitivity of Mueller-matrix for examined sample under different incident angles when (a) the width W changes by 1 nm and (b) the height H changes by 1 nm.

The limit width that can be resolved by MSM under the influence of different noise levels was further investigated. We added different levels of Gaussian random noise to the Mueller-matrix images of the examined sample with different widths and used them as the measured signature to reconstruct W . Figure 6 illustrates the average relative reconstructed error of 50 reconstruction trials. As for Fig. 6, the horizontal axis indicates line widths, and the vertical axis indicates the relative reconstructed error. And the curves with different color in Fig. 6 denote the addition of different levels of noise. As can be observed, the error increases as the noise increases. It is due to an increase in noise will reduce the signal-to-noise ratio (SNR) of the signatures of the sample. So the limit size that can be resolved depends on the magnitude of the noise. According to Eq. (S6) in Supplement 1 of the measured Mueller-matrix of air, the standard deviation σ_{noise} of measurement noise for MSM can be estimated as 0.01. Consequently, for the curve with

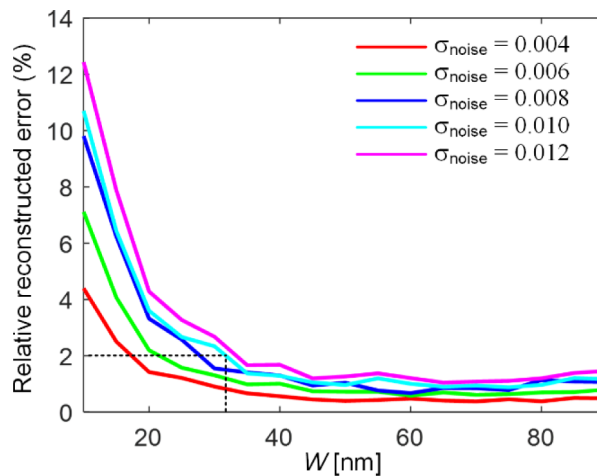


Fig. 6. The relative reconstructed error for different widths under different levels of noise. The reconstructed parameter is the width W .

$\sigma_{\text{noise}} = 0.01$, we take 2% relative reconstructed error as an example, one can see that the smallest size that can be resolved by MSM within 2% relative error is about 34 nm in theory.

4.2. Experimental results

Considering the measurement sensitivity of MSM is high at incident angles of 0° to about 20° according to Fig. 5, we first measured the Mueller-matrix images of the isolated Si lines sample at the normal incidence. As an example, Fig. 7 presents the measured Mueller-matrix image of the isolated Si line with a nominal width of 100 nm. As can be observed, there is an apparent ridge or valley shape that refers to the position of the isolated Si line in M_{34} and M_{43} , which has the highest SNR and contrast ratio between the isolated line and the substrate among all images. The line shape can also be observed in M_{33} and M_{44} but the contrast ratio is relatively low. And the SNR is relatively low in M_{12} and M_{21} . Note that, the two 2×2 off-diagonal blocks of the Mueller-matrix in Fig. 7 are not exactly equal to zeros due to the residual calibration errors and contamination such as dust on the sample. For each images of the Mueller matrix in Fig. 7, we select a rectangle region as indicated by the red dotted box shown in M_{34} , and extract the average pixel value along the vertical direction of the rectangle. The acquired one-dimensional Mueller-matrix distribution is then used for subsequent nanostructure reconstruction.

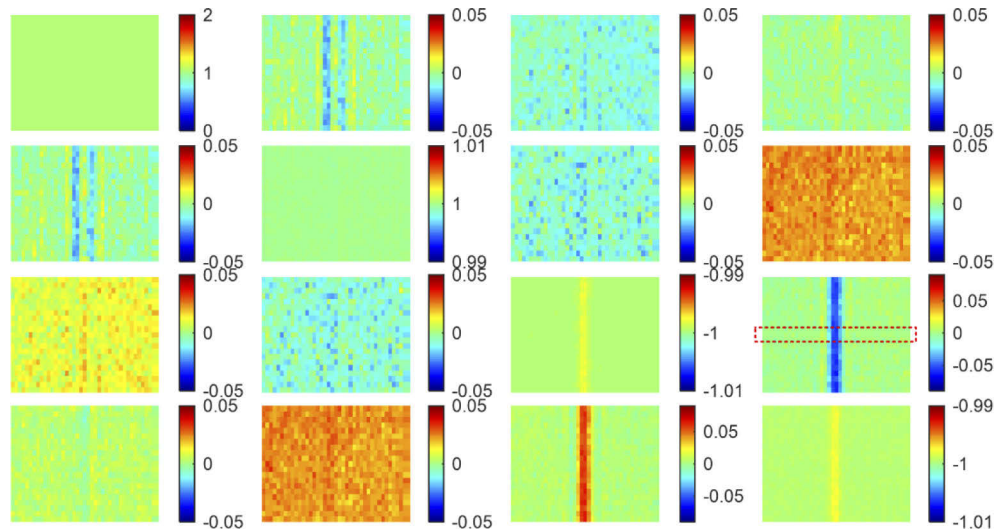


Fig. 7. The measured Mueller-matrix image of the isolated Si line with a nominal width of 100 nm at the normal incidence.

We use a geometric model shown in Fig. 8(a) in the forward model to measure the width W and the height H of the isolated Si line sample. Note that, as shown in Fig. 8(a), in the inverse reconstruction fitting process, we set not only W and H , but also the defocus D and the incident angle α to be floated. The purpose is to eliminate the effects of defocus in the measurement process and calibration errors in the incident angle to enable a better fitting of the calculated Mueller-matrix images to the measured data. After solving the inverse fitting according to this geometric model, the final fitting Mueller-matrix (i.e. the best-fit calculated Mueller-matrix to the measurement) of the isolated Si line with a nominal width of 100 nm at the normal incidence is shown in Fig. 8(b). The element m_{11} in Fig. 8(b) is omitted because it is normalized to one and is constant in the inverse fitting process. Great agreements between the measured data and the model for most elements can be observed in Fig. 8(b), especially in M_{34} and M_{43} . And M_{12} and M_{21} can match the measured signatures although their SNR is lower compared to M_{34} . Significant differences in measurement data and models can also be see for M_{24} and M_{42} . The

measured data of M_{24} and M_{42} are supposed to be zeros, and it is primarily due to the noise of the instrument in the measurement process. We also note that entire two 2×2 off-diagonal blocks of the fitting Mueller-matrix are zeros. It is because that the initial geometric model in Fig. 8(a) is set to be two-dimensional in the forward model and the direction of line extension is perpendicular to the plane of incidence. As a result, the W reconstructed by MSM is 106.90 ± 10.25 nm (with a 95% confidence interval). For comparison, the W measured by SEM is 100.90 ± 2.70 nm (with a 95% confidence interval). The relative error of MSM is 5.94% with respect to SEM. The fitting results of other isolated Si lines are presented in Figs. S4 ~ S7 in [Supplement 1](#).

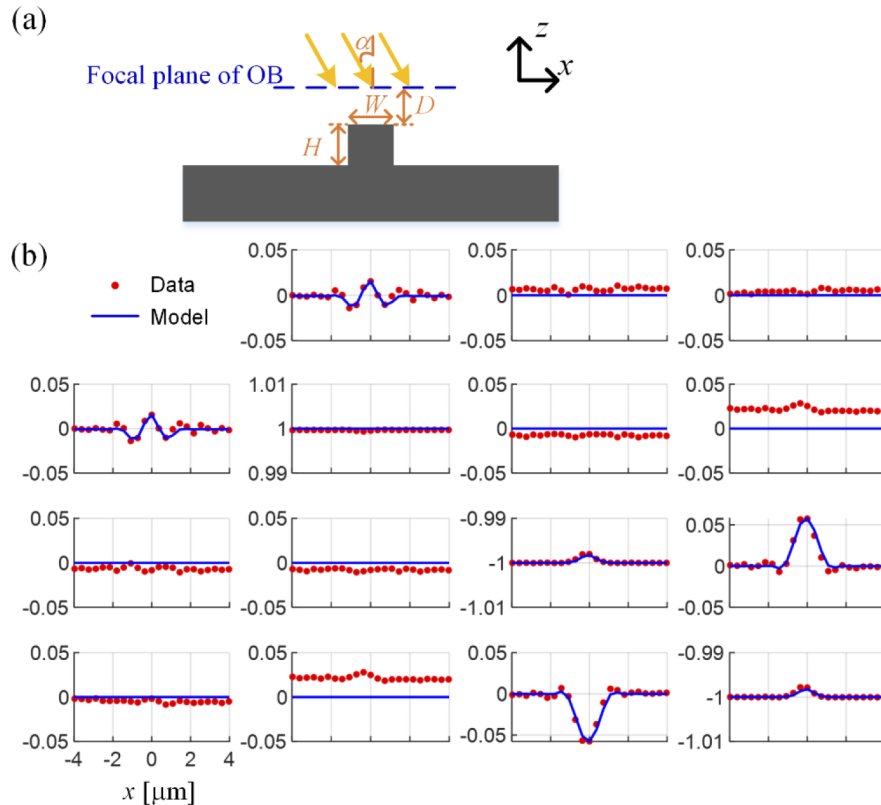


Fig. 8. (a) The geometric model of the investigated isolated Si line sample in the forward model; (b) The best-fit calculated and measured Mueller matrices of the isolated Si line with a nominal width of 100 nm at the normal incidence. The SEM- and MSM-measured widths W are 100.90 ± 2.70 nm and 106.90 ± 10.25 nm, respectively. The relative error is 5.94%.

Table 1 presents the comparison of parameters extracted from MSM and SEM measurements for different isolated lines. As can be observed from Table 1, compared with SEM measurements, the absolute error for W measured by MSM is less than about 7 nm for all lines. The corresponding relative error by MSM is less than 10% for the linewidth above 60 nm. However, the relative error of MSM is large for the isolated line with a nominal width of 20 nm. Figure S7 in [Supplement 1](#) shows that the SNR of the measured Mueller-matrix image is so low that the calculated Mueller matrices cannot match well with the measured ones for the isolated line with a nominal width 20 nm. This suggests that the sensitivity limit of MSM is about 40 nm, which is in accordance with the predicted limit in Fig. 6. It was revealed in Fig. 6 that the smallest size that can be resolved by MSM is about 34 nm within a 2% relative error. It is also noted from Table 1 that the H reconstructed by MSM are almost identical for lines with different widths except for 20 nm. All

the reconstructed defocus D are less than 3 μm . The reconstructed incident angles α are small due to the normal incidence.

Table 1. Comparison of parameters of isolated Si lines extracted from MSM and SEM measurements. The uncertainties appended to MSM- and SEM-measured values all have a 95% confidence level. The uncertainties associated with the SEM values were estimated in manually measuring the photographs

W by SEM [nm]	120.70 \pm 2.36	100.90 \pm 2.70	79.28 \pm 2.90	61.26 \pm 2.56	41.44 \pm 1.76	19.82 \pm 1.78
W by MSM [nm]	113.61 \pm 14.38	106.90 \pm 10.25	86.12 \pm 4.29	67.38 \pm 2.66	47.38 \pm 2.77	12.47 \pm 3.90
Relative Error	5.87%	5.94%	8.63%	9.98%	14.34%	37.06%
H by MSM [nm]	40.26 \pm 1.61	38.79 \pm 1.28	38.72 \pm 0.82	40.85 \pm 0.67	38.19 \pm 0.92	35.57 \pm 5.94
D by MSM [μm]	-0.88 \pm 0.17	-1.46 \pm 0.18	-0.43 \pm 0.14	-1.01 \pm 0.16	-0.38 \pm 0.21	2.36 \pm 0.72
α by MSM [deg]	-0.79 \pm 1.16	-2.18 \pm 0.55	-0.16 \pm 2.80	1.35 \pm 0.85	1.01 \pm 1.57	-1.00 \pm 1.05

Figure 9 presents a linear fit of the MSM-measured linewidths to those measured by SEM. In Fig. 9, the values on the horizontal and vertical axes of red dots represent the SEM and MSM measurements, respectively, and the corresponding error bars all have a 95% confidence interval. As can be observed, the coefficient of determination R^2 is 0.976 for the linewidths of 40 ~ 120 nm, which reveals a great correlation between the MSM- and SEM-measured results. As can also be seen from both Table 1 and Fig. 9, the uncertainties of W for MSM decrease as the width decreases, and are less than 3 nm for the linewidth of 40 ~ 60 nm, which closes to the uncertainties of SEM.

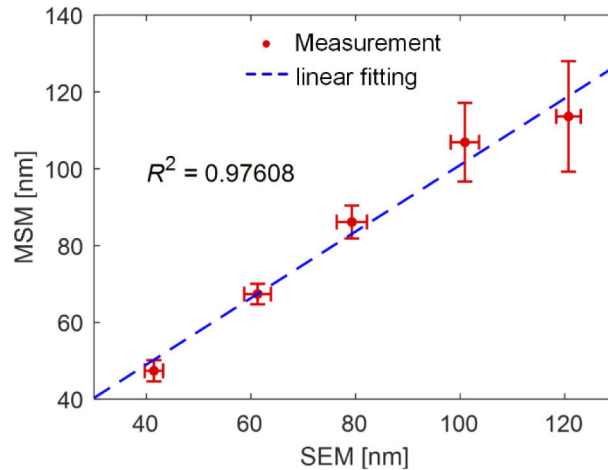


Fig. 9. The correlation between the MSM- and SEM-measured values of linewidth W . The associated error bars all correspond to a 95% confidence interval.

We then further examine the performance of MSM at other incident angles and the measurement results are presented in Section 4 of Supplement 1. Similarly, MSM-measured results shows a great agreement with those measured by SEM at these incident angles. It is also noted that the calculated Mueller matrices cannot match well with the measured ones and the corresponding reconstruction error increase significantly when the incident angle increases above 20°. It is primarily due to the sensitivity of MSM decreases with the incident angle beyond 20° as revealed in Fig. 5.

As summarized from the above results, it has been demonstrated that the proposed MSM can resolve a feature size of $\lambda/16$ with a sub-7 nm accuracy. In comparison with the related works on

measurement of finite subwavelength nanostructures, for instance, the scatterfield microscopy developed in Ref. [14] has demonstrated quantitative width measurement as small as 16 nm in size, namely $\lambda/30$ for 30-line arrays with uncertainties of 1 nm. In addition, Lee et al. proposed the application of a deformable mirror to through-focus scanning optical microscopy (TSOM), achieving an accuracy of less than 4 nm for the width of the isolated line sample in the range of 60 ~ 120 nm [16]. Although our accuracy and measurement limits are slightly less than these works, the scatterfield microscopy and TSOM both need scanning along the optical axis to acquire images at a large number of different focus positions, which would limit the efficiency and speed of measurement. In contrast, MSM takes less than 5 seconds for a single measurement and is thus more efficient.

The measurement capability of MSM far beyond the diffraction-limit is primarily attributed to the large amount of information and high sensitivity of Mueller-matrix image. The Mueller-matrix image of a sample is acquired by polarization modulation and demodulation, and represents the change of illuminating polarization state upon different features on the sample. So the morphological and structural information of the sample is encoded in its Mueller-matrix image. Besides, the proposed computational reconstruction strategy based on the established rigorous forward model of MSM fully explores the advantages of Mueller-matrix image. The key to the great performance of MSM include establishing a rigorous forward scattering model, precise calibration and measurement by the instruments, and considering multiple factors in solving the inverse problem.

The advantages of MSM are fast and non-destructive. The MSM is a computation-based method and need a priori knowledge of the sample. It is suitable for a wide range of finite nanostructures, such as nanowires in semiconductor devices. Besides, it can be used for process monitoring during production of the semiconductor industry. The proposed methodology can be easily extended to other optical imaging techniques to add the measured information, such as through-focus scanning microscopy [16], by introduction polarization modulation and demodulation and establishing a forward model of the corresponding optical system.

5. Conclusions

In conclusion, a novel approach that is capable of measuring finite nanostructures at deep sub-wavelength scale is proposed and demonstrated. The proposed approach relies on a computational reconstruction strategy and takes advantage of the large amount of information and high sensitivity of Mueller-matrix image to circumvent the diffraction-limit.

The developed MSM collects most of scattered-field by a high-NA objective lens, and acquires the Mueller-matrix image of the sample by polarization modulation and demodulation with two rotating phase retarders. We established a rigorous forward model for MSM that can calculate the Mueller-matrix image of the sample. The vectorial nature of the scattered field when passing through the imaging system and the effect of defocus in the measurement process are taken into account in the forward model. Besides, multiple factors including incident angle and defocus are considered in the inverse fitting process to enable a better fitting. The practical measurement capability is demonstrated by the experimental results on a series of isolated Si lines. It shows that the proposed MSM can resolve a feature size of $\lambda/16$ with sub-7 nm accuracy compared to SEM measurements. We believe that this work paves the way for a powerful and efficient characterization tool for future nanotechnology and nanoelectronics manufacturing.

Funding. National Natural Science Foundation of China (51775217, 51727809, 52022034); National Major Science and Technology Projects of China (2017ZX02101006-004); National Key Research and Development Program of China (2019YFB2005602); Key Research and Development Plan of Hubei Province (2020BAA008).

Disclosures. The authors declare that there are no conflicts of interest related to this article.

Data availability. Data underlying the results presented in this paper are not publicly available at this time but may be obtained from the authors upon reasonable request.

Supplemental document. See [Supplement 1](#) for supporting content.

References

1. T. Neuman, P. Alonso-González, A. Garcia-Etxarri, M. Schnell, R. Hillenbrand, and J. Aizpurua, "Mapping the near Fields of Plasmonic Nanoantennas by Scattering-Type Scanning near-Field Optical Microscopy," *Laser & Photonics Reviews* **9**(6), 637–649 (2015).
2. X. Hao, C. Kuang, Z. Gu, Y. Wang, S. Li, Y. Ku, Y. Li, J. Ge, and X. Liu, "From Microscopy to Nanoscopy via Visible Light," *Light: Sci. Appl.* **2**(10), e108 (2013).
3. N. Rotenberg and L. Kuipers, "Mapping Nanoscale Light Fields," *Nat. Photon.* **8**(12), 919–926 (2014).
4. J. N. Farahani, M. J. Schibler, and L. A. Bentolila, "Stimulated Emission Depletion (STED) Microscopy: from Theory to Practice," *Microsc. Sci. Technol. Appl. Educ.* **2**, 1539–1547 (2010).
5. P. Annibale, S. Vanni, M. Scarselli, U. Rothlisberger, and A. Radenovic, "Quantitative Photo Activated Localization Microscopy: Unraveling the Effects of Photoblinking," *PLoS One* **6**(7), e22678 (2011).
6. M. Saxena, G. Eluru, and S. Gorthi, "Structured illumination microscopy," *Adv. Opt. Photon.* **7**(2), 241–275 (2015).
7. M. G. L. Gustafsson, "Surpassing the lateral resolution limit by a factor of two using structured illumination microscopy," *J. Microsc.* **198**(2), 82–87 (2000).
8. C. Li, L. Han, H. Jiang, M. Jang, P. Lin, Q. Wu, M. Barnell, J. Yang, H. Xin, and Q. Xia, "Three-dimensional crossbar arrays of self-rectifying Si/SiO₂/Si memristors," *Nat. Commun.* **8**(1), 15666 (2017).
9. N. G. Orji, M. Badaroglu, B. M. Barnes, C. Beitia, B. D. Bunday, U. Celano, R. J. Kline, M. Neisser, Y. Obeng, and A. E. Vladar, "Metrology for the next generation of semiconductor devices," *Nat. Electron.* **1**(10), 532–547 (2018).
10. B. Tian, X. Zheng, T. J. Kempa, Y. Fang, N. Yu, G. Yu, J. Huang, and C. M. Lieber, "Coaxial silicon nanowires as solar cells and nanoelectronic power sources," *Nature* **449**(7164), 885–889 (2007).
11. T. Tajiri, S. Takahashi, Y. Ota, K. Watanabe, S. Iwamoto, and Y. Arakawa, "Three-dimensional photonic crystal simultaneously integrating a nanocavity laser and waveguides," *Optica* **6**(3), 296–299 (2019).
12. A. V. Kildishev, A. Boltasseva, and V. M. Shalaev, "Planar Photonics with Metasurfaces," *Science* **339**(6125), 1232009 (2013).
13. S. Arhab, G. Soriano, Y. Ruan, G. Ruan, A. Maire, D. Talneau, P. C. Sentenac, K. Chaumet, H. Belkebir, and Giovannini, "Nanometric Resolution with Far-Field Optical Profilometry," *Phys. Rev. Lett.* **111**(5), 053902 (2013).
14. J. Qin, R. Silver, B. Barnes, H. Zhou, R. Dixon, and M. A. Henn, "Deep subwavelength nanometric image reconstruction using Fourier domain optical normalization," *Light Sci Appl* **5**(2), e16038 (2016).
15. R. Chen, M. Wu, J. Ling, Z. Wei, Z. Chen, M. Hong, and X. Chen, "Superresolution microscopy imaging based on full-wave modeling and image reconstruction," *Optica* **3**(12), 1339–1347 (2016).
16. J. Lee, B. You, S. Park, and H. Kim, "Motion-free TSOM using a deformable mirror," *Opt. Express* **28**(11), 16352–16362 (2020).
17. K. Serrels, E. Ramsay, R. Warburton, and D. T. Reid, "Nanoscale optical microscopy in the vectorial focusing regime," *Nature Photon* **2**(5), 311–314 (2008).
18. N. Hafi, M. Grunwald, L. S. Heuvel, T. Aspelmeyer, J. Chen, M. Zagrebelsky, O. M. Schütte, C. Steinem, M. Korte, A. Munk, and P. J. Walla, "Fluorescence nanoscopy by polarization modulation and polarization angle narrowing," *Nat. Methods* **11**(5), 579–584 (2014).
19. K. Zhanghao, L. Chen, X. Yang, M. Wang, Z. Jing, H. Han, M. Q. Zhang, D. Jin, J. Gao, and P. Xi, "Super-resolution dipole orientation mapping via polarization demodulation," *Light Sci Appl* **5**(10), e16166 (2016).
20. D. Artigas, D. Merino, C. Polzer, and P. Loza-Alvarez, "Sub-diffraction discrimination with polarization-resolved two-photon excited fluorescence microscopy," *Optica* **4**(8), 911–918 (2017).
21. S. Liu, X. Chen, and C. Zhang, "Development of a broadband Mueller matrix ellipsometer as a powerful tool for nanostructure metrology," *Thin Solid Films* **584**, 176–185 (2015).
22. B. Richards and E. Wolf, "Electromagnetic Diffraction in Optical Systems. II. Structure of the Image Field in an Aplanatic System," *Proc. R. Soc. Lond. A* **253**(1274), 358–379 (1959).
23. E. Wolf, "Electromagnetic diffraction in optical systems. I. An integral representation of the image field," *Proc. R. Soc. Lond. A* **253**(1274), 349–357 (1959).
24. H. P. Urbach and S. F. Pereira, "Field in Focus with a Maximum Longitudinal Electric Component," *Phys. Rev. Lett.* **100**(12), 123904 (2008).
25. L. Li, "New formulation of the Fourier modal method for crossed surface-relief gratings," *J. Opt. Soc. Am. A* **14**(10), 2758–2767 (1997).
26. C. Wang, X. Chen, H. Gu, H. Jiang, C. Zhang, and S. Liu, "On the limits of low-numerical-aperture imaging scatterometry," *Opt. Express* **28**(6), 8445–8462 (2020).
27. V. F. Paz, S. Peterhansel, K. Frenner, and W. Osten, "Solving the inverse grating problem by white light interference Fourier scatterometry," *Light Sci Appl* **1**(11), e36 (2012).
28. M. Madsen, P. Hansen, M. Zalkovskij, M. Karamehmedović, and J. Garnæs, "Fast characterization of moving samples with nano-textured surfaces," *Optica* **2**(4), 301–306 (2015).
29. W. H. Press, S. A. Teukolsky, W. T. Vetterling, and B. P. Flannery, *Numerical Recipes: The Art of Scientific Computing*, 3rd ed. (Cambridge University, 2007), Chap. 15.
30. C. H. Herzinger, B. Johs, W. A. McGahan, J. A. Woollam, and W. Paulson, "Ellipsometric determination of optical constants for silicon and thermally grown silicon dioxide via a multi-sample, multi-wavelength, multiangle investigation," *J. Appl. Phys.* **83**(6), 3323–3336 (1998).

Reconstruction of finite deep sub-wavelength nanostructures by Mueller-matrix scattered-field microscopy: supplement

CAI WANG,¹ XIUGUO CHEN,^{1,*}  CHAO CHEN,¹ SHENG SHENG,¹
LIXUAN SONG,¹ HONGGANG GU,¹  HAO JIANG,¹  CHUANWEI
ZHANG,¹ AND SHIYUAN LIU^{1,2} 

¹State Key Laboratory of Digital Manufacturing Equipment and Technology, Huazhong University of Science and Technology, Wuhan, Hubei 430074, China

²shyliu@hust.edu.cn

*xiuguochen@hust.edu.cn

This supplement published with Optica Publishing Group on 22 September 2021 by The Authors under the terms of the [Creative Commons Attribution 4.0 License](https://creativecommons.org/licenses/by/4.0/) in the format provided by the authors and unedited. Further distribution of this work must maintain attribution to the author(s) and the published article's title, journal citation, and DOI.

Supplement DOI: <https://doi.org/10.6084/m9.figshare.16601921>

Parent Article DOI: <https://doi.org/10.1364/OE.432611>

Reconstruction of finite deep sub-wavelength nanostructures by Mueller-matrix scattered-field microscopy: supplemental document

1. Calibration and performance of MSM

In order to obtain accurate Mueller-matrices of a sample, it is necessary to perform calibrations for the optical elements in the MSM. The calibration consists of two steps. The first step involves the calibration of the polarizing elements and the beam splitter. The second step involves the calibration of the polarization aberration of the high-NA objective lens.

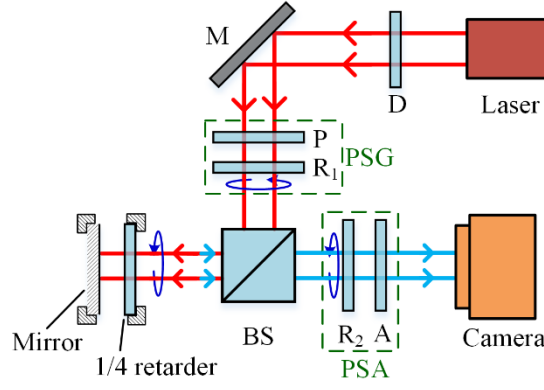


Fig. S1. The setup of the first step of calibration for the polarizing elements and beam splitter.

For the first step, as shown in Fig. S1, we remove OB, L_1 , L_2 and L_3 from MSM, and use a 1/4 retarder and a flat mirror as the calibration sample. Note that the Mueller-matrix of the flat mirror at normal incidence is always a diagonal matrix with diagonal elements being $(1, 1, -1, -1)$ [1]. In the calibration, the calibration sample can be rotated from its initial position at equal intervals. Assume that the beam splitter BS is isotropic and can be fully characterized by two ellipsometric parameters, i.e., the angles of amplitude ratio and phase difference. Hence, the calibration parameters include the transmission-axis orientations P and A of the polarizer P and analyzer A , the initial fast-axis orientations C_1 and C_2 and phase retardances δ_1 and δ_2 of the two phase retarders R_1 and R_2 , the angles of amplitude ratio Ψ_{bt} and Ψ_{br} and phase difference Δ_{bt} and Δ_{br} of the beam splitter BS in transmission and reflection, as well as the initial fast-axis orientation C_s and phase retardance δ_s of the 1/4 retarder. In the Stokes-Mueller formalism, the calibration setup shown in Fig. S1 can be described as

$$\mathbf{S}_{out} = \mathbf{M}_A(A)\mathbf{M}_R(C_2, \delta_2)\mathbf{M}_{bt}(\Psi_{bt}, \Delta_{bt})\mathbf{M}_S(C_s, \delta_s)\mathbf{M}_{br}(\Psi_{br}, \Delta_{br})\mathbf{M}_R(C_1, \delta_1)\mathbf{M}_P(P)\mathbf{S}_{in}, \quad (S1)$$

where \mathbf{S}_{in} and \mathbf{S}_{out} denote the Stoke vectors of the incoming and existing light, \mathbf{M}_P , \mathbf{M}_A , \mathbf{M}_R and \mathbf{M}_S represent the Mueller-matrices of the polarizer, analyzer, phase retarders, and calibration sample, respectively, \mathbf{M}_{br} and \mathbf{M}_{bt} are the Mueller-matrices of the beam splitter in reflection and transmission modes, respectively. According to Eq. (S1), the collected intensity corresponding to the m -th ($m = 1, 2, 3, \dots$) rotation position of the calibration sample can be expressed as [2]

$$I_{out,m} = I_{0,m} \left[1 + \sum_{n=1}^{16} (\alpha_{2n,m} \cos 2n\omega t + \beta_{2n,m} \sin 2n\omega t) \right], \quad (S2)$$

where $\{I_{0,m}, (\alpha_{2n,m}, \beta_{2n,m}), n = 1, 2, \dots, 16\}$ are the Fourier coefficients of the modulated light intensity $I_{out,m}$. For brevity, we denote the calibration parameters as a column vector $\boldsymbol{\eta} = [P, A,$

$C_1, C_2, C_s, \delta_1, \delta_2, \delta_s, \Psi_{bt}, \Psi_{br}, \Delta_{bt}, \Delta_{br}]^T$. The Fourier coefficients of the modulated light intensity at different rotation positions of the calibration sample compose another column vector $\mathbf{F} = [\alpha_{2n,m}, \beta_{2n,m}]^T$. Consequently, the calibration parameters can be acquired by solving the following optimization problem

$$\arg \min_{\boldsymbol{\eta}} (\|\mathbf{F}^{\text{calc}}(\boldsymbol{\eta}) - \mathbf{F}^{\text{meas}}\|_2), \quad (\text{S3})$$

where $\|\cdot\|_2$ denotes L₂-norm, \mathbf{F}^{calc} and \mathbf{F}^{meas} correspond to the column vectors that consist of the Fourier coefficients calculated according to Eqs. (S1) - (S2) and the Fourier coefficients estimated from the actually collected modulated light intensity in experiments, respectively.

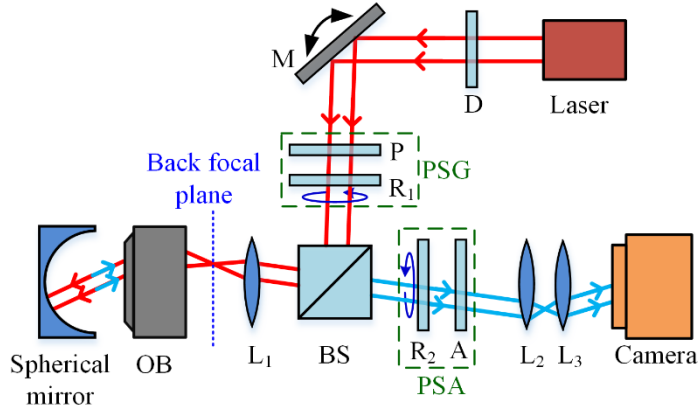


Fig. S2. The setup of the second step of the calibration for the high-NA objective lens.

As for the second step, we use a spherical mirror (SM) as the calibration sample. As shown in Fig. S2, the center of the SM is placed to coincide with the front focal point of the OB to guarantee that the illuminating light is normally incident upon the SM. Besides, the illumination direction of the light after the OB can be scanned from 0° to maximum determined by the NA of the OB by rotating the mirror, then we can calibrate the polarization effect of OB at different illumination directions. Assume that the constituent materials of OB are reciprocal. Ignore the polarization effects of lens L_1 , L_2 and L_3 due to their low NAs. Hence, for an arbitrary illumination direction, the sample Mueller matrix \mathbf{M}'_s here can be expressed as follows [3]

$$\mathbf{M}'_s = \mathbf{M}_{OB} \mathbf{M}_{SM} \mathbf{M}_{OB}, \quad (\text{S4})$$

where $\mathbf{M}_{SM} = \text{diag}(1, 1, -1, -1)$ is the Mueller-matrix of the SM, and \mathbf{M}_{OB} denotes the Mueller-matrix of the OB. Note that \mathbf{M}_s is acquired with the parameters calibrated in the first step. Then \mathbf{M}_{OB} can be obtained by

$$\mathbf{M}_{OB} = (\mathbf{M}'_s \mathbf{M}_{SM})^{1/2} \mathbf{M}_{SM}^{-1}. \quad (\text{S5})$$

To evaluate the accuracy and performance of MSM after the above two-step calibration, we measured the Mueller matrix of air using the calibrated MSM and obtained

$$\mathbf{M}_{\text{air}} = \begin{bmatrix} 1 & -0.0028 & 0.0006 & 0.0040 \\ -0.0029 & 0.9998 & 0.0017 & -0.0174 \\ -0.0006 & 0.0017 & 1.0000 & 0.0006 \\ -0.0039 & -0.0174 & -0.0006 & 0.9998 \end{bmatrix}. \quad (\text{S6})$$

As we know, the ideal Mueller matrix of air is $\text{diag}(1, 1, 1, 1)$. As a result, the bias of most Mueller matrix elements is less than 0.01 and the largest bias is 0.0174.

2. Forward model

In order to acquire the vectorial electric field and Mueller-matrix distribution on the image plane, it is necessary to calculate the electric field distribution on the entrance and exit pupil. Let us start with the scattered field $\mathbf{E}^0 = (E_s^0, E_p^0)$ of one of scattered lights with wave vector $\hat{\mathbf{q}} = (q_x, q_y, q_z)$ calculated by RCWA algorithm [4]. In order to simulate finite nanostructures, we set the length of the periodic unit to be large enough compared to the wavelength in the RCWA algorithm. As Fig. S3 shows, only the scattered lights within the numerical aperture (NA) of objective lens can be collected. According to the principles of Fourier optics [5], when the sample is located at a distance Δz from the focal plane of the objective lens, the electric field of $\hat{\mathbf{q}}$ on the entrance pupil can be obtained by

$$\mathbf{E}^{\text{entrance}} = e^{ik \cdot q_z \cdot \Delta z} \cdot P \cdot \mathbf{E}^0, \quad (\text{S7})$$

where $k = 2\pi/\lambda$ is the wave number; λ is the illuminating wavelength; i is the imaginary unit defined as $i^2 = -1$. And P in Eq. (S7) is a pupil function defined as follow

$$P = \begin{cases} 1, & (q_x^2 + q_y^2) \leq NA^2 \\ 0, & \text{else} \end{cases}. \quad (\text{S8})$$

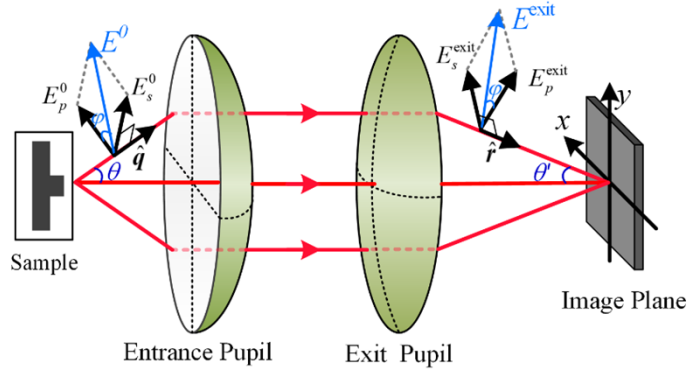


Fig. S3. The schematic of scattered light passing through the optical imaging system.

As shown in Fig. S3, the angle between $\hat{\mathbf{q}}$ and the optical axis is assumed to be θ . When the scattered light passing through the imaging system, the wave vector $\hat{\mathbf{q}}$ will rotate to $\hat{\mathbf{r}}$. The corresponding angles for $\hat{\mathbf{r}}$ is denoted as θ' . According to Abbe's theory [6], an aplanatic imaging system satisfies the following equations

$$n' \sin \theta' = \frac{n \sin \theta}{M}, \quad (\text{S9})$$

where n and n' is the refractive index in the object and image side respectively, and M is the magnification factor of the imaging system.

It is noted that in Fig. S3, the electric field components of the scattered light will rotate along with the wave vector. Besides, the amplitude of the electric field will also change due to the amplification effect of the imaging system. The electric field on the exit pupil can be obtained according to the law of energy conservation as follows [7]

$$\mathbf{E}^{\text{exit}} = -M \sqrt{\frac{n' \cos \theta'}{n \cos \theta}} \cdot \mathbf{E}^{\text{entrance}}. \quad (\text{S10})$$

3. Reconstruction results of different isolated lines

Figures S4 ~ S7 present the best-fit calculated and measured Mueller-matrices of isolated Si lines with nominal widths of 80 nm, 60 nm, 40 nm, and 20 nm, respectively, at the normal incidence. The uncertainties associated with the MSM- and SEM-measured values all have a 95% confidence level. We can observe that the match is well for the lines of 40 ~ 80 nm. In comparison, the single-to-noise ratio is poor for the line of 20 nm and the corresponding fitting error is large.

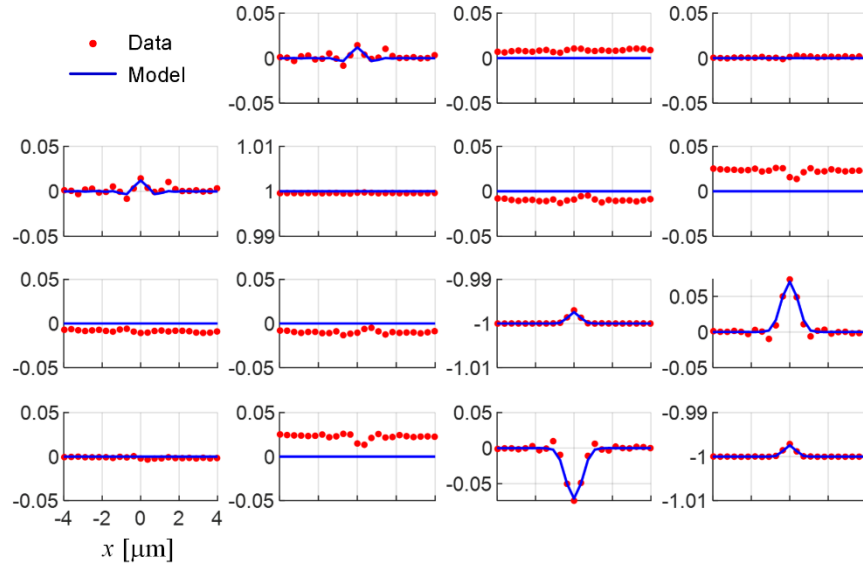


Fig. S4. The best-fit calculated and measured Mueller-matrix of the isolated Si line with a nominal width of 80 nm. The SEM- and MSM-measured widths W are 79.28 ± 2.90 nm and 86.12 ± 4.29 nm, respectively. The relative error is 8.63%.

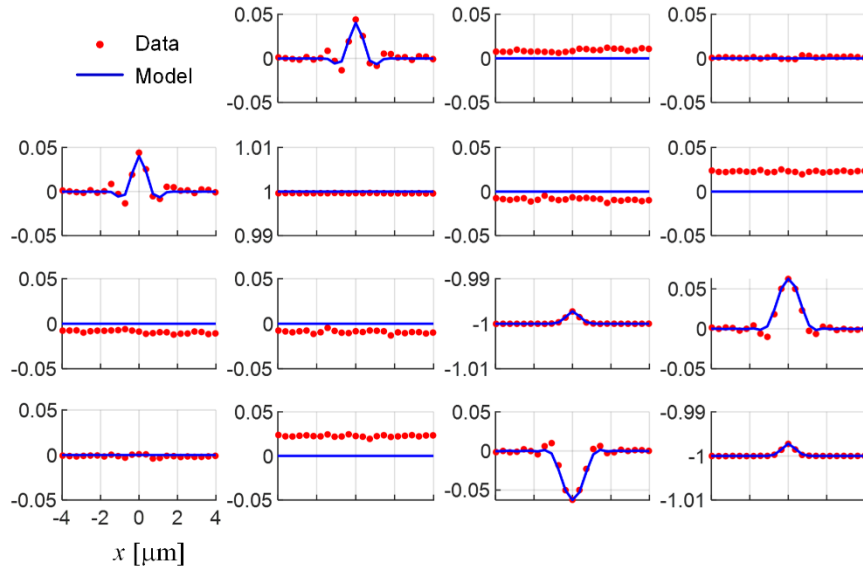


Fig. S5. The best-fit calculated and measured Mueller-matrix of the isolated Si line with a nominal width of 60 nm. The SEM- and MSM-measured widths W are 61.26 ± 2.56 nm and 67.38 ± 2.66 nm, respectively. The relative error is 9.98%.

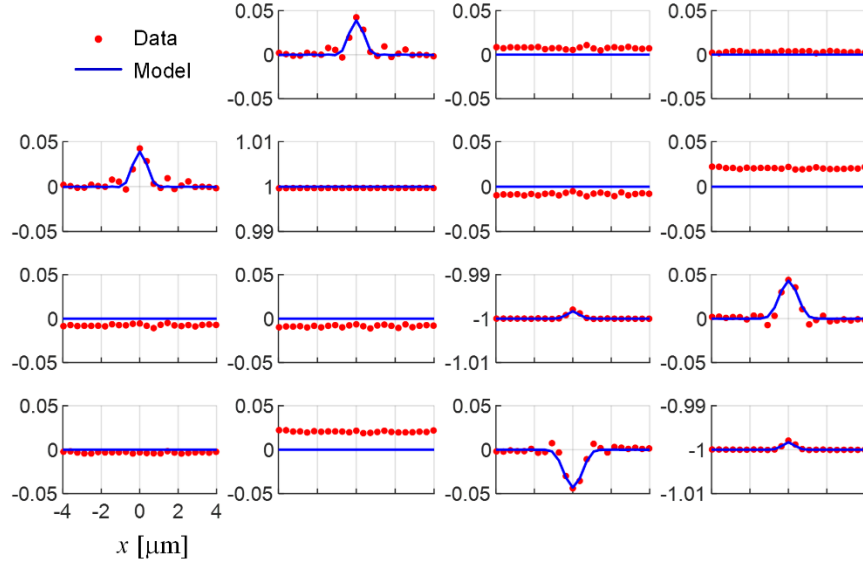


Fig. S6. The best-fit calculated and measured Mueller-matrix of the isolated Si line with a nominal width of 40 nm. The SEM- and MSM-measured widths W are 41.44 ± 1.76 nm and 47.38 ± 2.77 nm, respectively. The relative error is 14.34%.

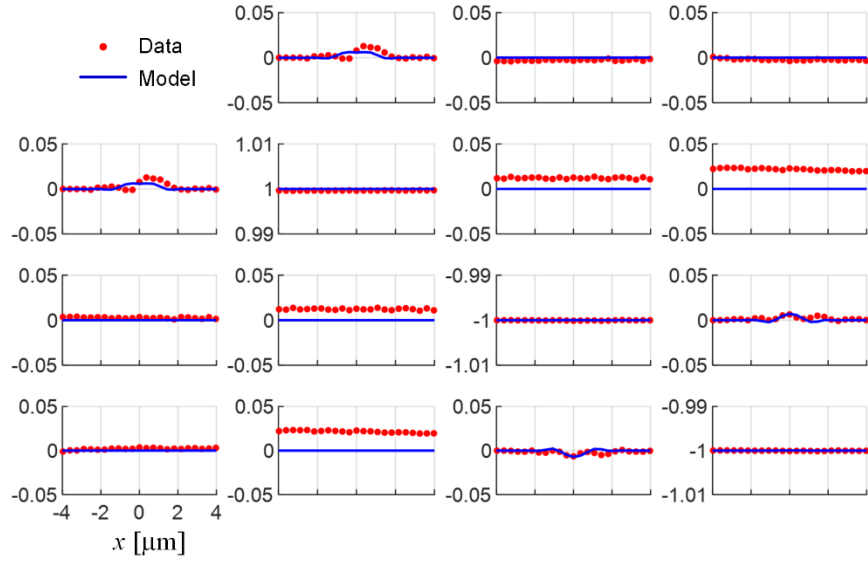


Fig. S7. The best-fit calculated and measured Mueller-matrix of the isolated Si line with a nominal width of 20 nm. The SEM- and MSM-measured widths W are 19.82 ± 1.78 nm and 12.47 ± 3.90 nm, respectively. The relative error is 37.06%.

4. Reconstruction results at different incident angles

Figures S8 – S10 present the reconstruction results of the isolated Si line with a nominal width of 100 nm at incident angles of 10° , 14° and 20° , respectively. Figures S11 – S13 show the linear fitting between the MSM and SEM measurements under these different incident angles. The uncertainties associated with the MSM- and SEM-measured values all have a 95% confidence level.

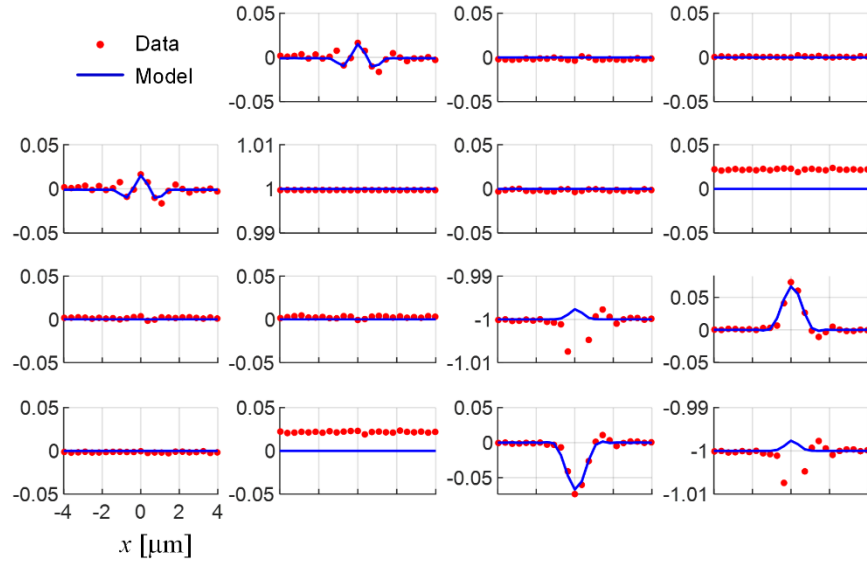


Fig. S8. The best-fit calculated and measured Mueller-matrix of the isolated Si line at the incident angle of 10° . The SEM- and MSM-measured widths W are 100.90 ± 2.70 nm and 98.39 ± 10.29 nm, respectively. The relative error is 2.49%.

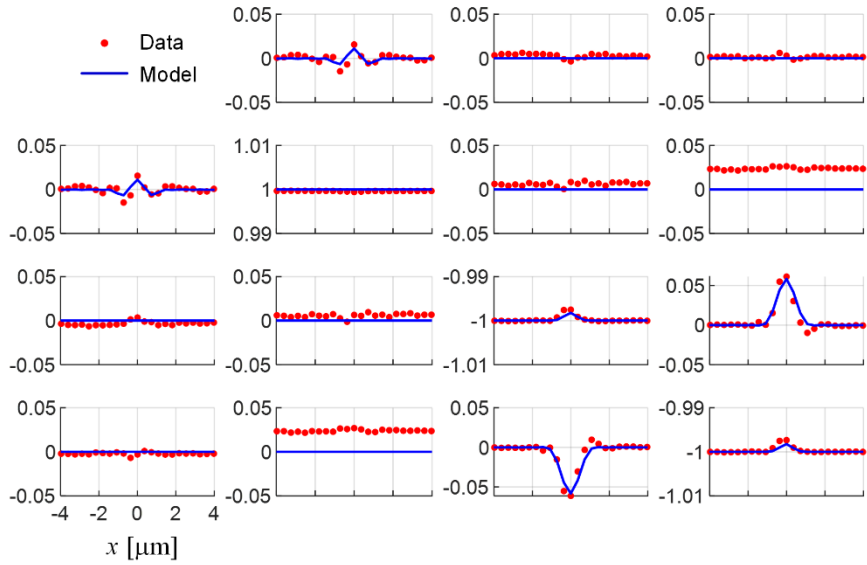


Fig. S9. The best-fit calculated and measured Mueller-matrix of the isolated Si line at the incident angle of 14° . The SEM- and MSM-measured widths W are 100.90 ± 2.70 nm and 96.65 ± 8.85 nm, respectively. The relative error is 4.21%.

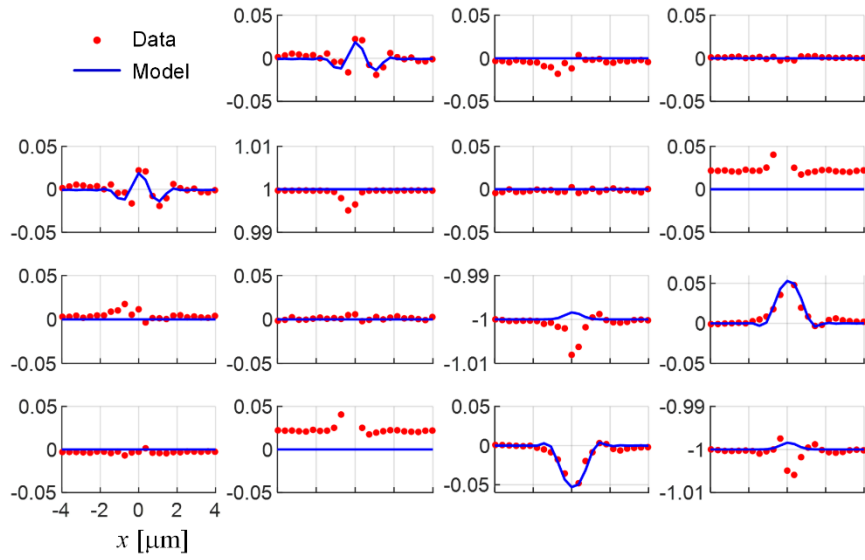


Fig. S10. The best-fit calculated and measured Mueller-matrix of the isolated Si line at the incident angle of 20° . The SEM- and MSM-measured widths W are 100.90 ± 2.70 nm and 104.27 ± 18.56 nm, respectively. The relative error is 3.33%.

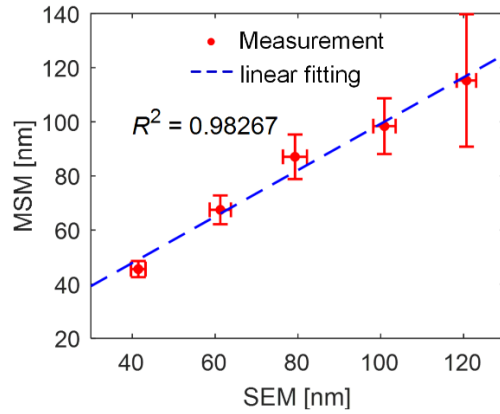


Fig. S11. The correlation between the MSM- and SEM-measured values of linewidth W at the incident angle of 10° .

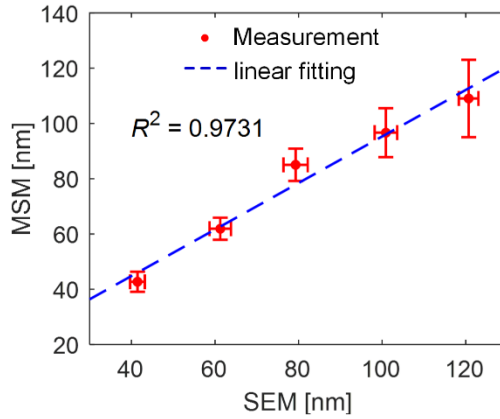


Fig. S12. The correlation between the MSM- and SEM-measured values of linewidth W at the incident angle of 14° .

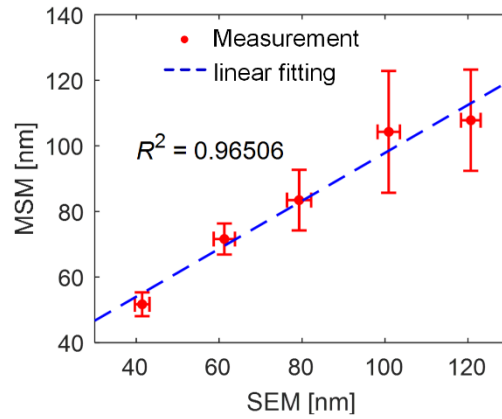


Fig. S13. The correlation between the MSM- and SEM-measured values of linewidth W at the incident angle of 20° .

Reference

1. D. H. Goldstein, *Polarized Light*, 3rd ed. (Boca Raton, FL: CRC Press, 2011).
2. S. Liu, X. Chen, and C. Zhang, "Development of a broadband Mueller matrix ellipsometer as a powerful tool for nanostructure metrology," *Thin Solid Films* **584**, 176-185 (2015).
3. C. Chen, X. Chen, H. Gu, H. Jiang, C. Zhang, and S. Liu, "Calibration of polarization effect of a high-numerical-aperture objective lens with Mueller matrix polarimetry," *Meas. Sci. Technol.* **30**, 025201 (2019).
4. L. Li, "New formulation of the Fourier modal method for crossed surface-relief gratings," *J. Opt. Soc. Am. A* **14**(10), 2758-2767 (1997).
5. J. W. Goodman, *Introduction to Fourier optics* (McGraw-Hill, 1968).
6. W. Singer, M. Totzeck, and H. Gross, *Physical Image Formation* (Wiley-VCH, 2005).
7. I. R. Capoglu, J. D. Rogers, A. Taflove, V. Backman, and E. Wolf, *Progress in Optics* (Elsevier, 2012), Chap. 1.